Why does rapid contraction of the radius of maximum wind precede rapid intensification in tropical cyclones?

Yuanlong Li[1,2], Yuqing Wang[3,4*], Yanluan Lin[1], Xin Wang[5]

[1]Ministry of Education Key Laboratory for Earth System Modeling, Department of Earth System Science, Tsinghua University, Beijing, China.

[2]School of Atmospheric Sciences, Nanjing University, Nanjing, China.

[3]International Pacific Research Center and Department of Atmospheric Sciences, School of Ocean and Earth Science and Technology, University of Hawaii at Mānoa, Honolulu, Hawaii, USA.

[4]State Key Laboratory of Severe Weather, Chinese Academy of Meteorological Sciences, China Meteorological Administration, Beijing, China.

[5]National satellite meteorological center of China meteorological administration, Beijing, China.

May 6, 2021 (submitted)

July 27, 2021 (revised)

Dateline

Submitted to ***Journal of the Atmospheric Sciences***

*Corresponding author address:
Prof. Yuqing Wang
International Pacific Research Center
University of Hawaii at Manoa
404A/POST, 1680 East West Road,
Honolulu, HI 96822, USA.
Email: yuqing@hawaii.edu

Abstract

The radius of maximum wind (RMW) has been found to contract rapidly well preceding rapid intensification in tropical cyclones (TCs) in recent literature but the understanding of the involved dynamics is incomplete. In this study, this phenomenon is revisited based on ensemble axisymmetric numerical simulations. Consistent with previous studies, because the absolute angular momentum (AAM) is not conserved following the RMW, the phenomenon can not be understood based on the AAM-based dynamics. Both budgets of tangential wind and the rate of change in the RMW are shown to provide dynamical insights into the simulated relationship between the rapid intensification and rapid RMW contraction. During the rapid RMW contraction stage, due to the weak TC intensity and large RMW, the moderate negative radial gradient of radial vorticity flux and small curvature of the radial distribution of tangential wind near the RMW favor rapid RMW contraction but weak diabatic heating far inside the RMW leads to weak low-level inflow and small radial absolute vorticity flux near the RMW and thus a relatively small intensification rate. As RMW contraction continues and TC intensity increases, diabatic heating inside the RMW and radial inflow near the RMW increase, leading to a substantial increase in radial absolute vorticity flux near the RMW and thus the rapid TC intensification. However, the RMW contraction rate decreases rapidly due to the rapid increase in the curvature of the radial distribution of tangential wind near the RMW as the TC intensifies rapidly and RMW decreases.

1. Introduction

Understanding the relationship between changes in intensity and the radius of maximum wind (RMW) in tropical cyclones (TCs) is important for understanding the dynamics of TC intensification because RMW contraction is often related to intensification (Shapiro and Willoughby 1982; Schubert and Hack 1982). Based on the balanced vortex dynamics, Shapiro and Willoughby (1982) showed that tangential wind tendency in response to diabatic heating in the eyewall is the greatest inside the RMW. This means that TC intensification and RMW contraction would occur simultaneously, as mentioned in many earlier observational studies (e.g., Willoughby et al. 1982; Willoughby 1990) and numerical studies (e.g., Judt and Chen 2013). However, more recent observational and numerical studies (Stern et al. 2015; Qin et al. 2016; Li et al. 2019) found that the RMW contraction often stops well before the end of intensification, which is in contrast with that implied by the result of Shapiro and Willoughby (1982). Stern et al. (2015) attributed the cessation of RMW contraction well before the end of intensification to the increased curvature of the radial distribution of tangential wind at the RMW as TC rapidly intensifies.

Another striking feature regarding the relationship between TC intensification and RMW contraction was recently documented by Wu and Ruan (2021), who showed that statistically rapid RMW contraction often precedes rapid intensification (RI) in observations. This phenomenon also appeared in many previous observational and numerical studies (e.g., Corbosiero et al. 2005, see their Fig. 4; Shimada and Horinouchi 2018, see their Fig. 7; Chen et al. 2011, see their Fig. 11; Stern et al. 2015, see their Fig. 4), but its dynamics did not receive any special attention in those studies. Results from statistical analyses for the North Atlantic TCs during 2000–2017 in Wu and Ruan (2021) revealed that rapid RMW contraction does not necessarily cause RI and generally only after the RMW contracts to a certain small size could a TC undergo RI. They found that the

TC intensification rate (IR) and the RMW contraction rate in the early intensification stage depend on the amount and radial location of convective heating inside the RMW and the size of the RMW. This dependence can be explained based on the tangential wind budget equation and balanced vortex dynamics (Schubert and Hack 1982). Namely, more convective heating inside the RMW drives stronger inflow to transport higher absolute angular momentum (AAM) inward to spin up the inner core in the lower troposphere; and the smaller RMW for a given intensity usually implies higher inner-core inertial stability and thus higher efficiency of eyewall heating in spinning up the inner core (Schubert and Hack 1982). However, Wu and Ruan (2021) did not provide any detailed insight into the dynamical processes that cause the rapid contraction preceding RI and they did not discuss what determines the amount and radial location of diabatic heating in the eyewall relative to the RMW.

In addition, many previous studies have qualitatively explained the relationship between TC intensification and RMW contraction based on the AAM-based dynamics (e.g., Holland and Merrill 1984; Pu et al. 2009; Chen et al. 2011, Kilroy et al. 2016). By this view, the RMW is assumed to be approximately a material surface, namely, the AAM following the RMW is nearly conserved during the RMW contraction and TC intensification. The AAM-based dynamics can be explained more transparently based on the AAM (M_m) passing through the RMW (r_m) as given below

$$M_m = r_m V_m + \frac{1}{2} f r_m^2, \tag{1}$$

where f is the Coriolis parameter, M_m and V_m are the AAM and the maximum tangential wind at r_m, respectively. Differentiating (1) with respect to time (τ) following the RMW, one can obtain

$$\frac{dV_m}{d\tau} = \left(\frac{V_m}{r_m} + f\right)\left(-\frac{dr_m}{d\tau}\right) + \frac{\dot{M}_m}{r_m}. \tag{2}$$

where $\dot{M}_m$ denotes the rate of change of M_m following the RMW. Note that both $dV_m/d\tau$ and

$dr_m/d\tau$ also follow the RMW rather than the air parcel. Equation (2) indicates that the RMW contraction ($-dr_m/d\tau > 0$) is associated with intensification as long as the AAM does not decrease too much following the RMW. Equation (2) also indicates that the contribution of RMW contraction to TC intensification depends on $V_m/r_m + f$, which is equivalent to the effect of inertial stability in the balanced vortex dynamics. If $\dot{M}_m$ is assumed to be small enough and omitted, Eq. (2) implies that the rapid TC intensification lags the rapid RMW contraction because the IR depends on not only the contraction rate but also the size of RMW and TC intensity. Namely, for the same RMW contraction rate, the weak intensity and large RMW are unfavorable for RI, or alternatively, RI may occur when the TC is strong enough with a relatively small RMW even the RMW contraction rate becomes small. This seems to provide a reasonable explanation for the observed relationship between TC intensification and RMW contraction as discussed in Wu and Ruan (2021) as well. However, Stern et al. (2015) showed that the AAM could change up to 50% following the RMW in their numerical simulated TCs, demonstrating that the RMW does not follow an AAM surface. Namely, $\dot{M}_m$ in Eq. (2) could not be ignored during TC intensification. Stern et al. (2015) found that the RMW first moves inward across AAM surfaces from higher to lower values of AAM during the initial rapid RMW contraction period, giving rise to negative $\dot{M}_m$ but once the RMW contraction ceases, AAM surfaces move inward across the RMW, corresponding to positive $\dot{M}_m$, and thus the TC continues to intensify more rapidly. This finding indicates that it is inappropriate to understand the relationship between TC intensification and RMW contraction solely based on the above AAM-based argument with the assumption of AAM being conserved along the RMW. Note that, here, it does not mean that any physical conservation law has been "violated", because the RMW itself is not a material surface but simply the location of a maximum in a scalar field as also suggested by Stern et al. (2015). Note that the negligible

$\dot{M}_m$ along the RMW was also assumed in the theoretical intensification model of Emanuel (2012). Therefore, it is necessary to provide a detailed evaluation of Eq. (2) during TC intensification.

In this study, the relationship between TC intensification and RMW contraction is revisited based on comprehensive diagnostics of ensemble axisymmetric numerical simulations of TC intensification. The main objectives are threefold: to provide an evaluation of the AAM-based dynamics using the simulation results, to examine how the amount and radial location of diabatic heating in the eyewall relative to the RMW evolve during the TC intensification, and to provide a more complete dynamical understanding of the relationship between TC intensification and RMW contraction based on the budgets for the RMW contraction and the tangential wind following the RMW. The rest of paper is organized as follow. Section 2 describes the model setup and experimental design. Section 3 provides an overview of the relationship between the RMW contraction and TC intensification in the ensemble simulations. The AAM-based dynamics of Eq. (2) is evaluated based on ensemble simulations in Section 4. Section 5 explains why the simulated rapid TC intensification lags the rapid RMW contraction based on the budgets of tangential wind and the rate of change in the RMW. Main conclusions are summarized in the last section.

2. Model setup and experimental design

The model used in this study is the axisymmetric version of the nonhydrostatic Cloud Model (CM1), version 19.8 (Bryan and Fritsch 2002), with the detailed model setup described in Li et al. (2020b). The model domain extends radially up to 3100 km with the grid spacing of 1 km within 100-km radius and linearly stretched to 12 km at the lateral boundary. The model atmosphere has 59 vertical levels with stretched grids below 5.5 km and uniform grid spacing of 500 m above. An f plane with the Coriolis parameter of 5×10^{-5} s^{-1} is assumed. The cloud microphysics parameterization is the double-moment scheme of Thompson et al. (2008), and no cumulus convective parameterization is used. The Newtonian cooling capped at 2 K day^{-1} is used to mimic the radiative cooling (Rotunno and Emanuel 1987), and dissipative heating is not considered in this study. The horizontal and asymptotic vertical mixing lengths are set at 700 m and 70 m, respectively. The surface enthalpy exchange coefficient is constant of 1.2×10^{-3}, and the surface drag coefficient depends on surface wind speed as given in Donelan et al. (2004). The sea surface temperature (SST)-dependent sounding experiments in Li et al. (2020b) are used, in which the atmospheric sounding for each SST bin is sorted from reanalysis data to ensure the consistency between SST and initial atmospheric sounding as in nature. There are four SST ensemble experiments with their corresponding atmospheric soundings sorted from the western North Pacific (WNP; labeled as SST28_WNP–SST31_WNP), and four experiments with their corresponding atmospheric soundings sorted from the North Atlantic (NA; labeled as SST27_NA–SST30_NA). For more details on the sounding construction, the readers are referred to Li et al. (2020b). Note that some of the simulation results were also used in Wang et al. (2021) to validate an energetically based TC intensification dynamical system model.

Each ensemble experiment has 21 simulations. The radial profile of the initial tangential wind is given following Wood and White (2011). In the standard run, the initial maximum tangential wind speed is 15 m s^{-1} with the initial RMW of 80 km at the surface and decreases linearly with height to zero at about 18 km. In the other 20 runs, the initial maximum tangential wind speed and the initial RMW are consecutively perturbed by the increments of ±0.1 m s^{-1} (for 10 runs) and ±0.4 km (for 10 runs), respectively. The simulation time for each run is 240 hours with the model output saved at every 10 min for budget analyses. To avoid the impacts of small-scale processes on TC IR or contraction rate, we only focus on the ensemble mean results as in Li et al. (2020b) and Wang et al. (2021). Note that for each experiment, although the timing of contraction and intensification varies among those ensemble runs (cf. Fig. 4 in Wang et al. 2021), our preliminary results have indicated that the ensemble mean results discussed here are insensitive to the perturbation increments within reasonable ranges.

3. An overview of the ensemble simulation results

The radius-time Hovmöller plots of the ensemble-mean AAM and tangential wind at 2-km height for each experiment are shown in Fig. 1. The 2-km height is used as in Stern et al. (2015) because we focus on the low-level flow but try to avoid the effects of unbalanced boundary-layer flow and vertical mixing on the AAM following the RMW. It can be seen from Fig. 1 that for each experiment, there is an initial adjustment period, during which a weak initial vortex core weakens and a new inner vortex occurs with a rapid, discontinuous contraction of the RMW. To avoid the impact of the adjustment period on the analysis of the primary intensification period, we only focus on the primary intensification phase, namely the period after the initial discontinuous RMW contraction and the new inner vortex attains an intensity of 12 m s^{-1} (results are insensitive to this threshold) as marked by the first horizontal purple line in Fig. 1 until the end of the simulated TC intensification (as the first time at which the ensemble mean intensity change rate attains zero) as marked by the second horizontal purple line in Fig. 1. During the earlier stage of this primary intensification period, the RMW first contracts slowly or barely changes with a relatively slow IR (compared to the peak rate of intensification). Subsequently, the RMW contracts rapidly and then the RMW contraction rate slows down and approaches zero finally. The IR still increases during the late stage of RMW contraction, as implied by the increasing density of the contours of tangential wind speed. This means that the change rates of the simulated TC intensity and RMW are not simultaneous, and the rapid contraction precedes the RI.

A closer comparison between the TC IR and change rate of RMW at 2-km height in each experiment is shown in Figs. 2a,b. Note that the small-scale perturbations of tangential wind less than 6 h in time and less than 8 km in radial direction are filtered out similar to Stern et al. (2015) and Li et al. (2019). The "tendencies" of the intensity and RMW refer to the rates of their changes in the subsequent 6 h forward difference after filtering rather than 24 h used in the observational study of Wu and Ruan (2021). As expected, the peak of RMW contraction rate is prior to the peak of IR in all experiments, indicating that the rapid contraction precedes the RI. Note that the "rapid" periods for both the IR and RMW contraction rates refer to the periods around their corresponding peaks and are not defined based on any specific threshold. Figures 2c,d show the TC IR and the rate of change of RMW based on the filtered tangential wind averaged the layer between the surface and 500 m height. Note that as done above, the initial adjustment period and the period after the end of intensification are not shown. Overall, the results are similar to those at 2-km height shown in Figs. 2a,b. Namely, the peak of contraction rate occurs prior to the peak of IR by about 10 h to more than 40 h, consistent with the observations documented in Wu and Ruan (2021). Furthermore, with the decrease in the time to attain the RI as SST increases, the time between the peak of RMW contraction rate and the peak of IR also decreases. This may be partly because the inner-core diabatic heating increases more rapidly with higher SST (Črnivec et al. 2016), and thus earlier RI following the RMW rapid contraction. In addition, the RMW contraction tends to cease (as the contraction rate attains zero) well before the end of intensification in all experiments no matter above or within the boundary layer, consistent with previous observational and numerical studies (Qin et al. 2016; Stern et al. 2015; Li et al. 2019).

We can see from Fig. 1 that the AAM following the RMW is not conserved, which is in contrast with the assumption in some previous studies (e.g., Holland and Merrill 1984; Emanuel 2012). As we can see more clearly from Figs. 3a,b, in the very beginning of the primary intensification stage as the RMW contracts slowly or barely changes, the AAM following the RMW increases by roughly 30–50%. However, subsequently the AAM following the RMW decreases by roughly 20–40% with the rapid RMW contraction. Then, as the contraction rate slows down, the AAM following the RMW increases again by about 20–60%. These are generally consistent with those found by Stern et al. (2015). As a result, although the AAM surface at the current RMW contracts in the following 6 h during the primary intensification stage (Fig. 1; Figs. 3c,d) as the RMW contracts (Figs. 2a,b), they contract at different rates (Figs. 3e,f). Note that assuming the RMW propagates continuously, the AAM surface at the current RMW must contract if there is intensification. The contraction rate of the AAM surface is much smaller than that of the RMW during the rapid contraction phase (Figs. 3e,f), and the peak of the AAM surface contraction rate generally lags the peak of the RMW contraction rate (Figs. 3c,d), suggesting that the term $\dot{M}_m/r_m$ in Eq. (2) is nonnegligible following the RMW. Therefore, the relationship between the TC intensification and RMW contraction could not be understood simply based on the conservation of AAM following the RMW as hypothesized in some previous studies (e.g., Holland and Merrill 1984; Pu et al. 2009; Chen et al. 2011; Kilroy et al. 2016; Emanuel 2012). This will be further quantitatively evaluated based on the results at the 2-km height in the next section.

4. An evaluation of the AAM-based dynamics

As mentioned above, based on Eq. (2), if the effect of $\dot{M}_m$ is omitted, the slow IR during the rapid contraction phase could be considered as a result of small $V_m/r_m + f$, and the RI during the slow contraction period could be considered as a result of the increased $V_m/r_m + f$. As shown in Figs. 4a,b, $V_m/r_m + f$ is indeed small during the rapid contraction phase because of the large RMW and weak TC intensity in all experiments, and then $V_m/r_m + f$ increases with the decrease of RMW. To evaluate the AAM-based dynamics, the simulated IR, the diagnosed IR from Eq. (2), and the contributions by the RMW contraction $[(V_m/r_m + f)(-dr_m/d\tau)]$ and $\dot{M}_m$ $(\dot{M}_m/r_m)$ are shown in Figs. 4c–h. Note that the simulated $dr_m/d\tau$ and $\dot{M}_m$ at each time τ_0 are calculated as the change rate of r_m and M_m between τ_0 and $\tau_0 + 6h$, and the V_m and r_m on the rhs of Eq. (2) are their averages between τ_0 and $\tau_0 + 6h$ based on the model outputs at 10-min intervals. As expected, the evolution and magnitude of the diagnosed IR are comparable well with that of the simulated IR in all experiments (Figs. 4c,d). However, although $V_m/r_m + f$ is small during the rapid contraction phase (Figs. 4a,b), the rapid contraction still implies a large IR (Figs. 4e,f). The RMW contraction-implied IR decreases with the decreasing RMW contraction rate (Figs. 4e,f) although $V_m/r_m + f$ shows considerable increase due to the TC intensification (Figs. 4a,b). This means that the evolution of the diagnosed IR associated with the RMW contraction during the early intensification stage is generally similar to the evolution of the RMW contraction rate. However, this is in contrast with the evolution of the simulated IR, suggesting that the term associated with the RMW contraction in Eq. (2) could not determine the simulated IR alone. This is because the diagnosed IR due to $\dot{M}_m/r_m$ is negative during the rapid contraction phase in all experiments, showing a minimum at the peak of the RMW contraction rate (Figs. 4g,h). The negative $\dot{M}_m/r_m$ during the rapid contraction phase is consistent with the decrease of AAM following the RMW as mentioned earlier (Fig. 1; Figs. 3a,b). As the contraction rate slows down, the diagnosed IR due to $\dot{M}_m/r_m$ increases gradually and becomes positive, consistent with the increase of the simulated IR (Figs. 4c,d). The diagnosed IR due to $\dot{M}_m/r_m$ shows a great contribution to the peak of the simulated IR (Figs. 4g,h).

The above analysis indicates that the simulated slow IR during the rapid contraction phase is mainly associated with the decrease of AAM following the RMW, and the simulated RI during the slow contraction phase is largely associated with the increase of AAM following the RMW. This means that $\dot{M}_m$ is not negligible following the RMW and is key to the lag of the RI behind the rapid RMW contraction in the AAM-based dynamics. Therefore, it is inappropriate to explain the relationship between RMW contraction and TC intensification by omitting the effect of $\dot{M}_m$ as assumed in many previous studies (e.g., Holland and Merrill 1984; Pu et al. 2009; Chen et al. 2011, Emanuel 2012; Kilroy et al. 2016). Note that $\dot{M}_m$ itself is a function of TC IR and RMW contraction rate by definition. Therefore, the AAM-based dynamics provides little insights into the physical/dynamical understanding on the relationship between TC intensification and RMW contraction.

5. New insights from tangential wind and RMW budgets

To help understand the relationship between the simulated TC intensification and RMW contraction during the primary intensification stage after the initial adjustment, we conducted the budgets for both tangential wind and the rate of change in the RMW as done in Li et al. (2019), with the results discussed in this section. Note that the present study focuses on the early intensification stage based on the ensemble-mean budget results, rather than the late intensification stage based on the single simulation results in Li et al. (2019). The tangential wind tendency equation in the axisymmetric, cylindrical coordinates can be written as (Li et al. 2019, 2020a)

$$\frac{\partial V_m}{\partial \tau} = -u_m \xi_{a,m} - w_m \frac{\partial V_m}{\partial z} + F_{h,m} + F_{v,m}, \tag{3}$$

where the subscript "m" denotes the variables at the RMW, u and w denote radial wind and vertical velocity, $\xi_a = \partial v/\partial r + v/r + f$ denotes absolute vertical vorticity. Note that at the RMW, the radial gradient of tangential wind is zero by definition and thus ξ_a equals to $V_m/r_m + f$, which also appears in Eq. (2). The terms on the rhs of Eq. (3) denote the radial (horizontal) flux of absolute vorticity (ADV_H), vertical advection (ADV_V), radial diffusion due to subgrid-scale horizontal mixing (DIFF_H), and vertical diffusion due to turbulent mixing including surface friction (DIFF_V). As in Li et al. (2019, 2020a), all instantaneous terms in Eq. (3) are directly from the model output and thus ideally no computational error in the budget is introduced.

The diagnostic equation for the RMW contraction rate, based on the kinematic/geometric definition of the RMW, can be given below following Stern et al. (2015),

$$\frac{d\mathrm{RMW}}{d\tau} = -\frac{(\partial/\partial r)(\partial V_m/\partial \tau)}{\partial^2 V_m/\partial r^2}, \tag{4}$$

where the numerator and denominator on the rhs denote the radial gradient of tangential wind tendency and the curvature of the radial distribution of tangential wind at the RMW, respectively. Because of the negative definite nature of the curvature at the RMW, the sign of the RMW tendency depends on the radial gradient of tangential wind tendency. Substituting the tangential wind tendency equation (3) into Eq. (4), we get (Li et al. 2019)

$$\frac{d\mathrm{RMW}}{d\tau} = \frac{(\partial/\partial r)(u_m \xi_{a,m})}{\partial^2 V_m/\partial r^2} + \frac{(\partial/\partial r)\left(w_m \frac{\partial V_m}{\partial z}\right)}{\partial^2 V_m/\partial r^2} - \frac{(\partial/\partial r)(F_{h,m})}{\partial^2 V_m/\partial r^2} - \frac{(\partial/\partial r)(F_{v,m})}{\partial^2 V_m/\partial r^2}. \tag{5}$$

The terms on the rhs of Eq. (5) denote contributions of the radial gradient of tangential wind tendency to the RMW tendency due to radial flux of absolute vorticity (ADV_H_S15), vertical advection (ADV_V_S15), radial diffusion (DIFF_H_S15), and vertical diffusion including surface friction (DIFF_V_S15).

Equations (3) and (5) can be used to understand the relationship between TC intensification and RMW contraction. Considering that the eyewall above the boundary layer is spun up by the vertical advection of AAM from the boundary layer (e.g., Zhang et al. 2001; Heng and Wang 2016; Peng et al. 2018; Li et al. 2019, 2020a) and the RMW within the boundary layer also influences the RMW above the boundary layer (Stern et al. 2014, 2015), we focus on the RMW tendency and tangential wind tendency below 500-m height in the boundary layer as in Li et al. (2019). Similar to Stern et al. (2015) and Li et al. (2019), the small-scale features in the vertically-averaged tangential wind as well as those tangential wind tendency terms in the rhs of Eq. (3) with time scales less than 6 h and radial scales less than 8 km are filtered out. Similarly, the simulated TC IR and $d\mathrm{RMW}/d\tau$ at each time τ_0 are calculated as the change rate of TC intensity and RMW between τ_0 and $\tau_0 + 6h$, and all budget terms for both tangential wind and RMW tendencies are their averages between τ_0 and $\tau_0 + 6h$ using the model outputs at 10-min intervals.

Figures 5 and 6 show the budget results using Eqs. (3) and (5), respectively. We can see that both the simulated TC IR and RMW contraction rate in all experiments are well captured by the budgets based on Eq. (3) and Eq. (5) (Figs. 5a,b; Figs. 6a,b), implying that the model outputs at 10-min intervals can be used to examine the time evolution of TC intensity and RMW contraction. As shown in previous studies (e.g., Zhang et al. 2001; Heng and Wang 2016; Li et al. 2019, 2020a), the radial vorticity flux dominates the inner-core spinup in the boundary layer (Figs. 5c,d), and all the vertical advection and diffusion terms including surface friction contribute to the inner-core spindown in the boundary layer (Figs. 5e–j). This means that the TC IR largely depends on the radial vorticity flux, which is determined by the secondary circulation (u_m), TC intensity (V_m), and the size of RMW (Eq. 3). Note that after the peak of IR, the simulated IR decreases (Figs. 5a,b) although the radial vorticity flux still rapidly increases (Figs. 5c,d). This is because the surface friction, which is approximately proportional to the square of the maximum tangential wind, also increases rapidly with the rapid increase of TC intensity (not shown). As a result, the associated negative contribution of vertical diffusion and vertical advection in the boundary layer to the IR also rapidly increases (Figs. 5e,f,i,j; Li et al. 2020a).

From Figs. 6c–j, we can see that the radial vorticity flux forcing dominates the RMW contraction rate (Figs. 6c,d) and the vertical advection forcing and the diffusion forcings (including surface friction) tend to reduce RMW contraction (Figs. 6e–j), consistent with the budget analyses of Li et al. (2019). During the late stage of TC intensification (after the peak of TC IR), the vertical advection forcing (Figs. 6e,f) decreases, the horizontal diffusion forcing (Figs. 6g,h) increases with the increasing TC intensity and contributes largely to the cessation of RMW contraction, and the vertical diffusion forcing including surface friction (Figs. 6i,j) also plays an important role in prohibiting RMW contraction. Note that although the direct effect of the vertical diffusion including surface friction on RMW contraction discussed here is negative, its net effect may be positive because surface friction would enhance the low-level radial vorticity flux and its negative radial gradient (Stern et al. 2015; Li et al. 2019, 2020a). Another striking feature of the budgets is that although the contribution of vertical diffusion including surface friction to the IR is much larger than that of horizontal diffusion (Figs. 5g–j), the contribution of vertical diffusion forcing to the RMW contraction rate is smaller than that of horizontal diffusion forcing (Figs. 6g–j) during the late stage of TC intensification. This is because the contours of the horizontal diffusion forcing are more parallel to the RMW than that of the vertical diffusion forcing (not shown, cf. Li et al. 2019), and thus the radial gradient of the horizontal diffusion is larger than that of the vertical diffusion as indicated in Li et al. (2019).

To address why the simulated rapid contraction precedes the RI, we mainly focus on the early intensification stage, the period after the initial adjustment and prior to the peak of the simulated IR, which includes the rapid contraction phase (cf. Figs. 5a,b; Figs. 6a,b). During the early intensification stage, the surface friction is relatively small because of the weak surface wind speed, and the simulated IR is dominated by the radial vorticity flux (Figs. 5c,d), which increases with the increasing TC intensity and the decreasing RMW. However, as the TC evolves, the increase in intensity and decrease in RMW would increase the curvature of the radial distribution of tangential wind and thus is unfavorable for the RMW contraction as implied by Eqs. (4) or (5) (Stern et al. 2015; Li et al. 2019) although the radial vorticity flux forcing, which dominates the RMW contraction, increases as the TC intensifies during the early intensification stage (Figs. 6c,d). During the rapid RMW contraction phase with slow TC intensification, the TC intensity is relatively weak and the RMW is relatively large (Figs. 7a,b), giving rise to a small curvature (Figs. 7e,f). As a result, even though the negative gradient of radial vorticity flux and thus the negative gradient of net tangential wind tendency near the RMW is moderate (Figs. 6c,d; Figs. 7e,f), it can induce a large RMW contraction rate (Figs. 6a,b). However, the small radial vorticity flux near the RMW (Figs. 5c,d) is unfavorable for the RI as implied by Eq. (3) (Figs. 5a,b). With the intensification of the TC and the continuous decrease of the RMW, the curvature of the radial distribution of tangential wind near the RMW increases continuously (Figs. 7e,f), leading to the slowdown of the RMW contraction (Figs. 6a,b). The small RMW and strong intensity during the slow contraction phase (Figs. 7c,d) are more favorable for RI than the relatively large RMW and weak intensity during the rapid RMW contraction phase (Figs. 7a,b).

In addition to the TC intensity and size of RMW, the radial vorticity flux also depends on the low-level inflow as inferred from Eq. (3), which is partly controlled by diabatic heating in the eyewall. It is our interest to further compare the TC structure and diabatic heating during different phases. Figure 8 shows the composite TC structures and diabatic heating rates at times when the RMW contraction rate (Fig. 8a) and the IR (Fig. 8b) reach their respective peaks among all experiments. Note that the composites are conducted here because the TC structures are similar among all experiments for both times (Figs. 7a–d). As expected, diabatic heating in the inner core and thus the low-level inflow are much weaker during the rapid RMW contraction phase than during the RI phase. Therefore, based on Eq. (3), during the rapid RMW contraction phase (Fig. 8a), the weak low-level inflow associated with weak diabatic heating inside the RMW, together with the relatively large RMW and weak TC intensity (Figs. 7a,b), results in weak low-level radial vorticity flux near the RMW and thus small IR. Note that here the weak diabatic heating is itself largely a reflection of the weak intensity. As the TC intensifies, the enhanced diabatic heating and thus low-level inflow, and the increasing TC intensity and decreasing RMW favor the high IR during the RI phase (Fig. 8b).

Furthermore, we can see from Figs. 8a and 8b that the maximum heating rate is located further inside the RMW during the rapid RMW contraction phase than during the RI period. This can be understood based on the boundary layer dynamics discussed in Kepert (2017), who revealed that the radial location of the eyewall updraft is a function of the RMW. The eyewall updraft in a larger RMW TC would be located more inside the RMW than in a smaller RMW TC (see also Li and Wang 2021). Consistently, the radial inflow also penetrates more inside the RMW in a large RMW TC than in a small RMW TC. Because the relatively high absolute vorticity inside the RMW, the more inwardly penetrated inflow would lead to relatively large tangential wind tendency also more inside the RMW, as implied by the balanced vortex dynamics (Shapiro and Willoughby 1982; Schubert and Hack 1982). This favors the contraction of the RMW but is less favorable for TC intensification because the tangential wind tendency near the RMW is relatively small. This point is illustrated by comparing the radial distributions of tangential wind and its tendency in the boundary layer at the time of the peak in RMW contraction rate and the time of the peak in IR shown in Figs. 8c and 8d. During the rapid RMW contraction phase, larger tangential wind tendencies are well inside the RMW, which contribute relatively small tangential wind increasing tendency near the RMW (Fig 8c) but contribute largely to the RMW contraction rate because of the small curvature of the radial distribution of tangential wind. However, with the decreasing RMW following the rapid contraction phase, the diabatic heating rate is larger and becomes closer to the RMW (Fig. 8b), this would induce much larger tangential wind tendencies near the RMW (Fig. 8d), contributing largely to the TC IR but little to the RMW contraction rate due to the large curvature of the radial distribution of tangential wind. These results further indicate that in addition to the dependence of the radial vorticity flux on TC intensity and the size of RMW (or the inertial stability in the inner core of the TC), the dependence of the strength and radial location of diabatic heating in the eyewall relative to the RMW on the size of the RMW and TC intensity is also a key to the simulated lag of RI behind the rapid RMW contraction. This latter dependence results primarily from the unbalanced boundary layer dynamics as discussed above (Kepert 2017) while the former dependence results mainly from the balanced vortex dynamics. Therefore, both balanced and unbalanced dynamics work cooperatively to determine the relationship between the simulated rapid RMW contraction and TC intensification.

6. Conclusions and discussion

In this study, the relationship between the TC IR and RMW contraction rate is revisited through ensemble numerical experiments using an axisymmetric cloud model. The focus is on the asynchrony between the rapid contraction and RI, namely, the rapid contraction precedes the RI, which has been reported in previous observational and numerical studies (e.g., Corbosiero et al. 2005; Chen et al. 2011; Stern et al. 2015; Wu and Ruan 2021) but the understanding of the involved dynamics is incomplete. Most previous studies explained the relationship between RMW contraction and TC intensification qualitatively based on the assumption of AAM-conservation following the RMW (e.g., Holland and Merrill 1984; Pu et al. 2009; Chen et al. 2011, Kilroy et al. 2016). Under this assumption, the IR would depend primarily on the RMW contraction rate. This hypothesis has been invalidated in a recent study based on high-resolution numerical simulations by Stern et al. (2015).

Our results show that the AAM following the RMW is not conserved and can vary by ~30–50% no matter during the rapid contraction phase or during the RI phase, consistent with the results of Stern et al. (2015). As a result, the IR of the simulated TC could not be diagnosed by the RMW contraction rate only because the RMW is not a material surface. During the rapid contraction phase, the RMW shifts rapidly inward across the AAM surfaces, namely the AAM following the RMW decreases with relatively small IR of the simulated TC. However, during the slow RMW contraction phase, the AAM surfaces moves inward passing through the RMW, corresponding to the high IR. Therefore, the AAM conservation following the RMW as assumed in previous TC intensification theory (e.g., Emanuel 2012) is not valid as also pointed out by Stern et al. (2015). The AAM-based diagnostics provides little physical/dynamical insights into the understanding of the relationship between TC IR and RMW contraction rate because the rate of change in AAM following the RMW needs to be explained.

To understand why the rapid RMW contraction precedes the RI in the simulated TCs, we performed both the tangential wind budget and the budget for the rate of change in RMW in the simulated TCs. Results show that during the rapid RMW contraction phase, the slow intensification is primarily due to the small radial vorticity flux near the RMW, while the rapid RMW contraction is largely due to the moderate negative radial gradient of the radial vorticity flux and the small curvature of the radial distribution of tangential wind near the RMW. The relatively small radial vorticity flux near the RMW results primarily from the weak TC intensity and large size of RMW (and thus weak inner-core inertial stability) and weak low-level inflow. The moderate radial gradient of the radial vorticity flux results primarily from the more inwardly displaced eyewall updraft (and thus convection) relative to the RMW due to more inwardly penetrated low-level inflow controlled by the boundary layer dynamics as proposed by Kepert (2017). With the decrease of RMW due to the rapid contraction and the increase of TC intensity, the inner-core inertial stability increases and the low-level inflow becomes less penetrative relative to the RMW, resulting in the eyewall updraft less inwardly displaced. As a result, the radial vorticity flux increases with the maximum slightly inside and close to the RMW, giving rise to high intensification rate and thus RI of the simulated TCs. Although during the RI phase, the negative radial gradient of the radial vorticity flux near the RMW is also large, the RMW contraction is greatly suppressed by the rapidly increasing curvature of the radial distribution of tangential wind.

Note that this study only discusses one scenario regarding the relationship between the rapid

RMW contraction and TC RI, i.e., with the rapid RMW contraction preceding RI. Wu and Ruan (2021) showed that there are also considerable portion of TCs experiencing rapid RMW contraction and RI simultaneously in observations. They found that those TCs are characterized by the combination of large RMW and sufficient convective heating close to the storm center (cf. their Fig. 12c). As shown in our idealized simulations, the large RMW always occurs during the earlier stage of the intensification period, however, during which the convective heating is often weak or not "sufficient". We thus hypothesize that in idealized conditions, it is easier for the rapid RMW contraction to precede RI than in nature, but this needs to be further examined in a future study. In addition, results from this study do not mean that there must be an RI (often quantitatively defined as the near-surface maximum wind speed increase more than 15 m s^{-1} per day; Kaplan and DeMaria 2003) following rapid RMW contraction, as mentioned earlier and in Wu and Ruan (2021). This is because in nature there are many deleterious environmental effects to TC intensification, such as vertical wind shear and oceanic cold core eddies, which are not included in our idealized simulations.

Note also that as our main conclusions in this study are based on the axisymmetric model experiments, it is unclear whether and how much the asymmetric eddy processes may contribute to the relationship between the RMW contraction and TC intensification rate. Nevertheless, since most of our results are consistent with previous three-dimensional model simulations (e.g., Stern et al. 2015; Li et al. 2019) and observations (Wu and Ruan 2021), our main conclusions could be also applicable to three-dimensional simulations. In addition, this study only provides some dynamical/physical insights into the relationship between the rapid RMW contraction and TC RI qualitatively. It will be a good topic for a future study to quantify the relationship, e.g., the lag time between the rapid RMW contraction and TC RI, so that the results can provide guidance to real-time TC intensity forecasts.

Acknowledgments: This study was supported in part by National Natural Science Foundation of China under grants 41730960 and the National Key R&D Program of China under grant 2017YFC1501602 and in part by NSF grant AGS-1834300. Y. Li is supported by the fellowship of China National Postdoctoral Program for Innovative Talents (No. BX2021121).

References

Bryan, G. H., and J. M. Fritsch, 2002: A benchmark simulation for moist nonhydrostatic numerical model. *Mon. Wea. Rev.*, **130**, 2917–2928, https://doi.org/10.1175/1520-0493(2002)130,2917: ABSFMN.2.0.CO;2.

Chen, H., D. Zhang, J. Carton, and R. Atlas, 2011: On the rapid intensification of Hurricane Wilma (2005). Part I: Model prediction and structural changes, *Wea. Forecasting*, **26**, 885-901, https://doi.org/10.1175/WAF-D-11-00001.1.

Corbosiero, K. L., J. Molinari, and M. L. Black, 2005: The structure and evolution of Hurricane Elena (1985). Part I: Symmetric intensification, *Mon. Wea. Rev.*, **133**, 2905-2921, https://doi.org/10.1175/MWR3010.1.

Črnivec, N., R. K. Smith, and G. Kilroy, 2016: Dependence of tropical cyclone intensification rate on sea-surface temperature. *Quart. J. Roy. Meteor. Soc.*, **142**, 1618–1627, https://doi.org/10.1002/qj.2752.

Donelan, M. A., B. K. Haus, N. Reul, W. J. Plant, M. Stiassnie, H. C. Graber, O. B. Brown, and E. S. Saltzman, 2004: On the limiting aerodynamic roughness of the ocean in very strong winds. *Geophys. Res. Lett*., **31**, L18306, https://doi.org/10.1029/ 2004GL019460.

Emanuel, K. A., 2012: Self-stratification of tropical cyclone outflow. Part II: Implications for storm intensification. *J. Atmos. Sci.*, **69**, 988– 996, https://doi.org/10.1175/JAS-D-11-0177.1.

Heng, J., and Y. Wang, 2016: Nonlinear response of a tropical cyclone vortex to prescribed eyewall heating with and without surface friction in TCM4: Implications for tropical cyclone intensification. *J. Atmos. Sci.*, **73**, 1315–1333, https://doi.org/10.1175/JAS-D-15-0164.1.

Holland, G. J., and R. T. Merrill, 1984: On the dynamics of tropical cyclone structural changes. *Quart. J. Roy. Meteor. Soc.*, **110**, 723–745, https://doi.org/10.1002/qj.49711046510.

Judt, F., and S. S. Chen, 2013: Reply to ‘‘Comments on ‘Convectively generated potential vorticity in rainbands and formation of the secondary eyewall in Hurricane Rita of 2005.’’’ *J. Atmos. Sci.,* **70**, 989–992, https://doi.org/10.1175/JAS-D-12-0151.1.

Kaplan, J., and M. DeMaria, 2003: Large-scale characteristics of rapidly intensifying tropical cyclones in the North Atlantic basin. *Wea. Forecasting*, **18**, 1093–1108, https://doi.org/10.1175/1520-0434(2003)018,1093: LCORIT.2.0.CO;2.

Kepert, J. D., 2017: Time and space scales in the tropical cyclone boundary layer, and the location of the eyewall updraft. *J. Atmos. Sci.*, **74**, 3305–3323, https://doi.org/10.1175/JAS-D-17-

0077.1.

Kilroy, G., R. K. Smith, and M. T. Montgomery, 2016: Why do model tropical cyclones grow progressively in size and decay in intensity after reaching maturity? *J. Atmos. Sci.*, **73**, 487–503, https://doi.org/10.1175/JAS-D-15-0157.1.

Li, T.-H., and Y. Wang, 2021: The role of boundary layer dynamics in tropical cyclone intensification. Part II: Sensitivity to initial vortex structure. *J. Meteor. Soc. Japan*, **99**, 537–554, https://doi.org/10.2151/jmsj.2021-028.

Li, Y., Y. Wang, and Y. Lin, 2019: Revisiting the dynamics of eyewall contraction of tropical cyclones. *J. Atmos. Sci.*, **76**, 3229–3245, https://doi.org/10.1175/JAS-D-19-0076.1.

Li, Y., Y. Wang, and Y. Lin, 2020a: How much does the upward advection of the supergradient component of boundary layer wind contribute to tropical cyclone intensification and maximum intensity? *J. Atmos. Sci.*, **77**, 2649–2664, https://doi.org/ 10.1175/JAS-D-19-0350.1.

Li, Y., Y. Wang, Y. Lin, and R. Fei, 2020b: Dependence of superintensity of tropical cyclones on SST in axisymmetric numerical simulations. *Mon. Wea. Rev.*, **148**, 4767-4781, https://doi.org/10.1175/MWR-D-20-0141.1.

Peng, K., R. Rotunno, and G. H. Bryan, 2018: Evaluation of a time- dependent model for the intensification of tropical cyclones. *J. Atmos. Sci.*, **75**, 2125–2138, https://doi.org/10.1175/JAS-D- 17-0382.1.

Pu, Z., X. Li, and E. J. Zipser, 2009: Diagnosis of the initial and forecast errors in the numerical simulation of the rapid intensification of Hurricane Emily (2005). *Wea. Forecasting*, **24**, 1236–1251, https://doi.org/10.1175/2009WAF2222195.1.

Qin, N., D.-L. Zhang, and Y. Li, 2016: A statistical analysis of steady eyewall sizes associated with rapidly intensifying hurricanes. *Wea. Forecasting*, **31**, 737–742, https://doi.org/10.1175/ WAF-D-16-0016.1.

Rotunno, R., and K. A. Emanuel, 1987: An air–sea interaction theory for tropical cyclones. Part II: Evolutionary study using a nonhydrostatic axisymmetric numerical model. *J. Atmos. Sci.*, **44**, 542–561, https://doi.org/10.1175/1520-0469(1987)044,0542: AAITFT.2.0.CO;2.

Schubert, W. H., and J. J. Hack, 1982: Inertial stability and tropical cyclone development. *J. Atmos. Sci.*, **39**, 1687–1697, https:// doi.org/10.1175/1520-0469(1982)039,1687:ISATCD.2.0.CO;2.

Shapiro, L. J., and H. E. Willoughby, 1982: The response of balanced hurricanes to local sources of heat and momentum. *J. Atmos. Sci.*, **39**, 378–394, https://doi.org/10.1175/1520-0469(1982)

039,0378:TROBHT.2.0.CO;2.

Shimada, U., and T. Horinouchi, 2018: Reintensification and eyewall formation in strong shear: A case study of Typhoon Noul (2015). *Mon. Wea. Rev.,* **146**, 2799-2817, https://doi.org/10.1175/MWR-D-18-0035.1.

Stern, D. P., J. R. Brisbois, and D. S. Nolan, 2014: An expanded dataset of hurricane eyewall sizes and slopes. *J. Atmos. Sci.*, **71**, 2747– 2762, https://doi.org/10.1175/JAS-D-13-0302.1.

Stern, D. P., J. L. Vigh, D. S. Nolan, and F. Zhang, 2015: Revisiting the relationship between eyewall contraction and intensification. *J. Atmos. Sci.*, **72**, 1283–1306, https://doi.org/ 10.1175/JAS-D-14-0261.1.

Thompson, G., P. R. Field, R. M. Rasmussen, and W. D. Hall, 2008: Explicit forecasts of winter precipitation using an improved bulk microphysics scheme. Part II: Implementation of a new snow parameterization. *Mon. Wea. Rev*., **136**, 5095–5115, https://doi.org/10.1175/2008MWR2387.1.

Willoughby, H. E., 1990: Temporal changes of the primary circulation in tropical cyclones. *J. Atmos. Sci.*, **47**, 242–264, https://doi.org/10.1175/1520-0469(1990)047,0242:TCOTPC. 2.0.CO;2.

Willoughby, H. E., J. A. Clos, and M. G. Shoreibah, 1982: Concentric eye walls, secondary wind maxima, and the evolution of the hurricane vortex. *J. Atmos. Sci*., **39**, 395–411, https://doi.org/10.1175/1520-0469(1982)039,0395:CEWSWM.2.0.CO;2.

Wang, Y., Y. Li, J. Xu, Z.-M. Tan, and Y. Lin, 2021: The intensity-dependence of tropical cyclone intensification rate in a simplified energetically based dynamical system model. *J. Atmos. Sci*., **78**, (in press), https://doi.org/10.1175/JAS-D-20-0393.1.

Wood, V. T., and L. W. White, 2011: A new parametric model of vortex tangential-wind profiles: Development, testing, and verification. *J. Atmos. Sci.*, **68**, 990–1006, https://doi.org/ 10.1175/2011JAS3588.1.

Wu, Q., and Z. Ruan, 2021: Rapid contraction of the radius of maximum tangential wind and rapid intensification of a tropical cyclone. *J. Geophys. Res. Atmos.*, **126**, e2020JD033681, https://doi.org/10.1029/2020JD033681.

Zhang, D., Y. Liu, and M. K. Yau, 2001: A multiscale numerical study of Hurricane Andrew (1992). Part IV: Unbalanced flows. *Mon. Wea. Rev.*, **129**, 92–107, https://doi.org/10.1175/ 1520-0493(2001)129,0092:AMNSOH.2.0.CO;2.

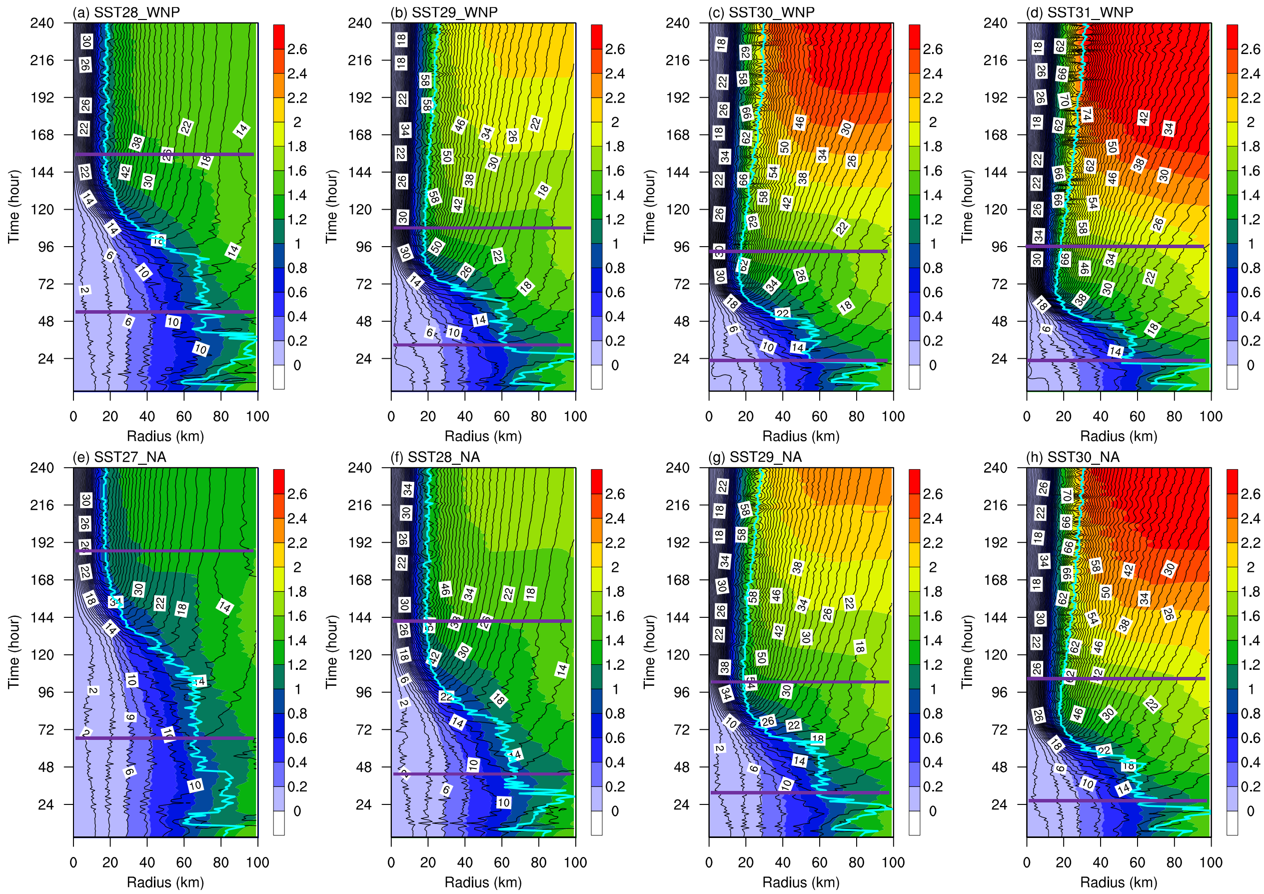

Figure 1. Radius-time Hovmöller plots of hourly ensemble-mean absolute angular momentum (shades; 10^6 m^2 s^{-1}) and tangential wind (contours; at an interval of 2 m s^{-1}) at 2-km height, overlaid by the radial position of RMW (cyan curve), and the two purple horizontal lines mark the intensification period after the initial adjustment in each experiment.

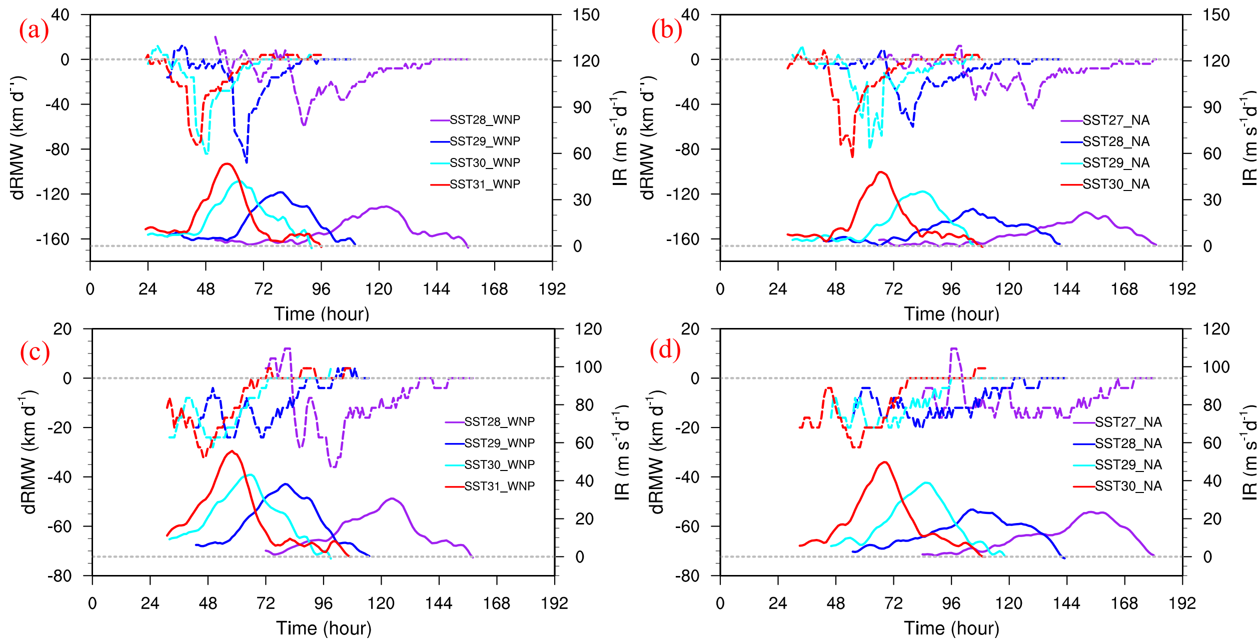

Figure 2. Time series of tendency of RMW (dRMW; dashed curves) and tendency of maximum tangential wind speed (IR; solid curves) (a,b) at 2-km height and (c,d) averaged below 500 m. Only results during the primary intensification period after the initial adjustment are shown.

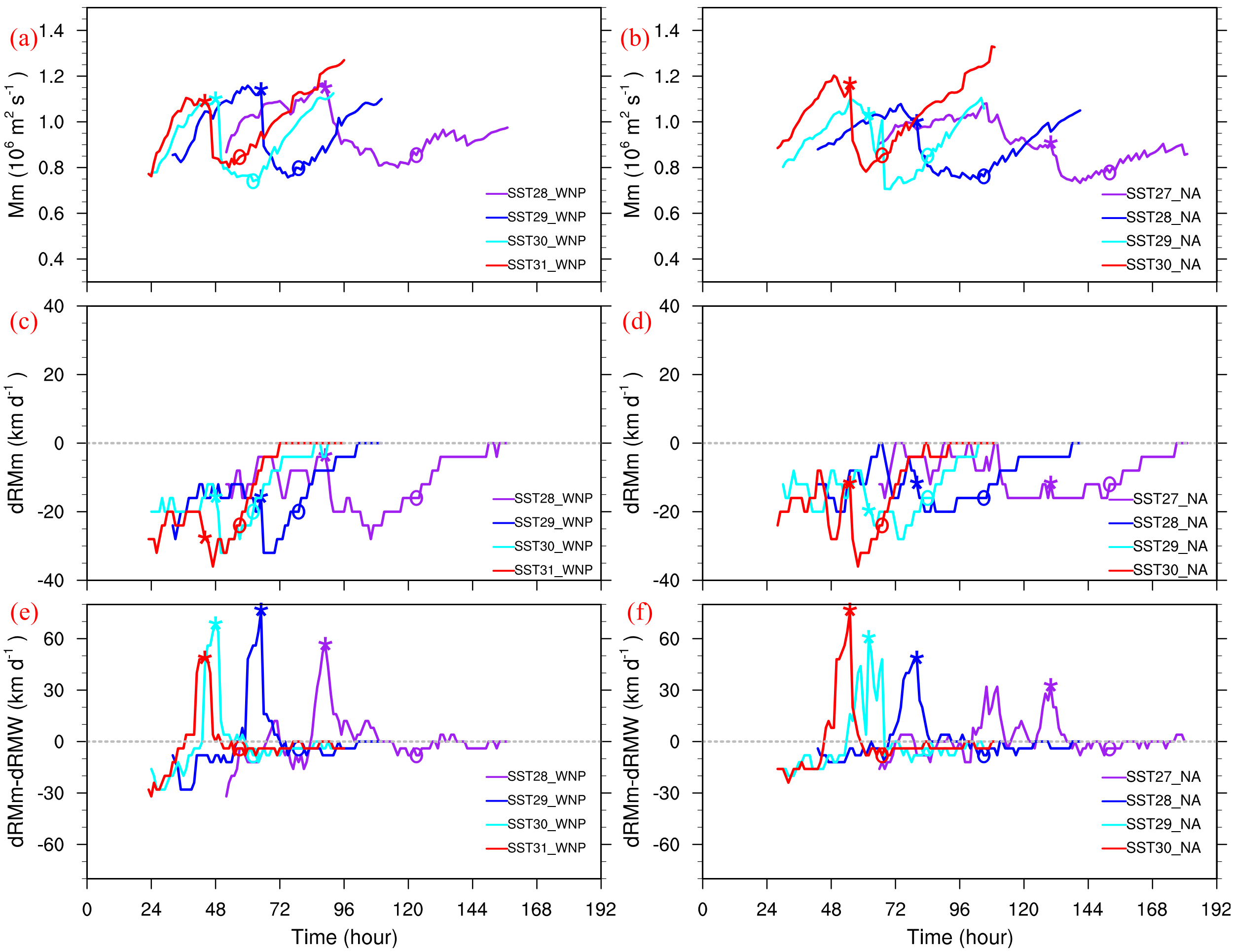

Figure 3. (a,b) Time series of absolute angular momentum following the RMW at 2-km height. (b,c) Time series of change rate in the radius of absolute angular momentum surface from the current RMW to the radius at the subsequent 6 h for the same absolute angular momentum surface (dRMm). (e,f) Time series of the difference between dRMm and dRMW. Only results during the primary intensification period after the initial adjustment are shown. The asterisk and circle on each curve mark the time of the peak RMW contraction rate and the time of the peak simulated IR, respectively.

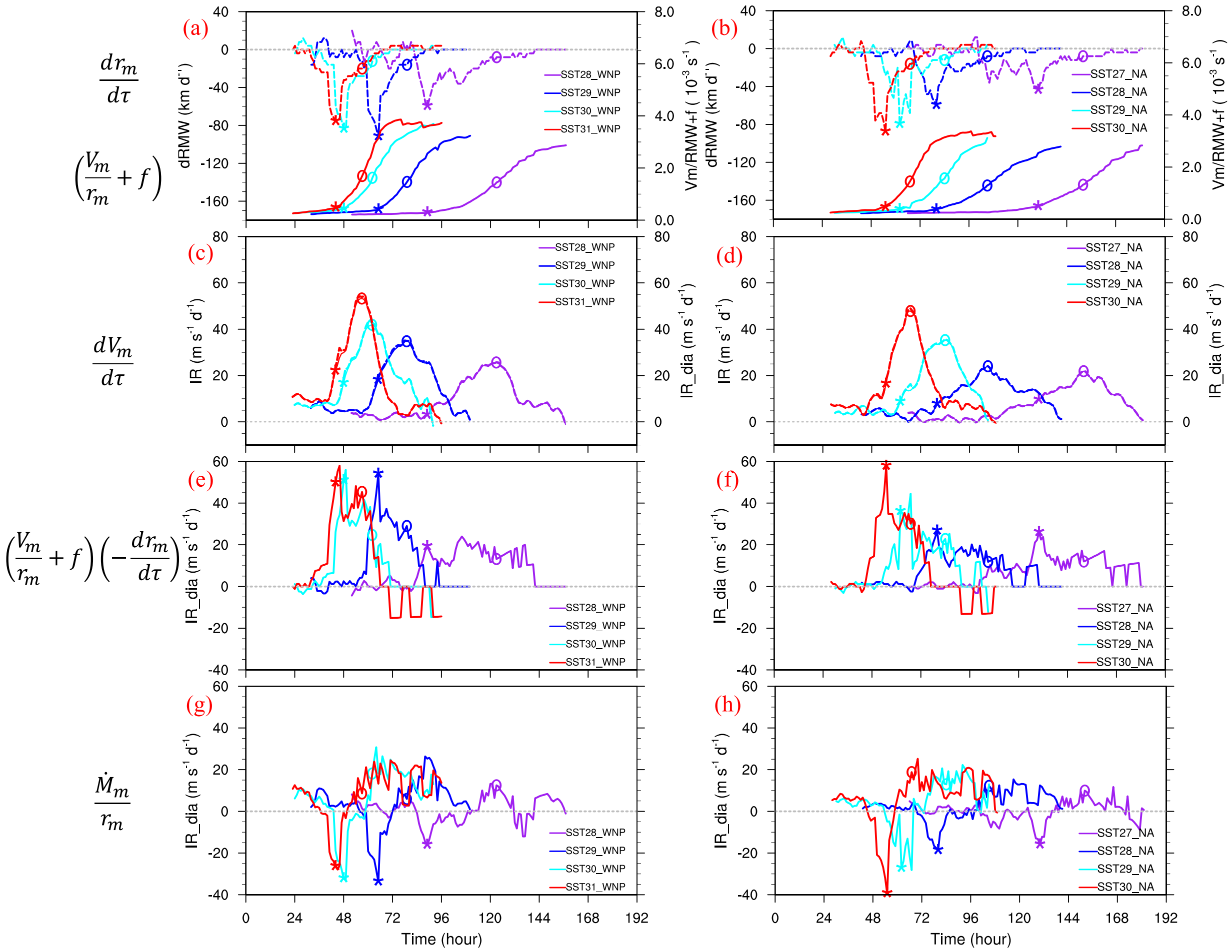

Figure 4. (a,b) Time series of tendency of RMW (dRMW; dashed curves) and $V_m/r_m + f$ (solid curves). (c,d) Time series of the simulated IR (solid curves) and diagnosed IR based on Eq. (2) (dashed curves). Note that the solid curves are mostly under the dashed curves. (e,f) Times series of $(V_m/r_m + f)(-dr_m/d\tau)$. (g,h) Times series of $\dot{M}_m/r_m$. All results are from 2-km height, and only results during the primary intensification period after the initial adjustment are shown. The asterisk and circle on each curve mark the time of the peak RMW contraction rate and the time of the peak simulated IR, respectively.

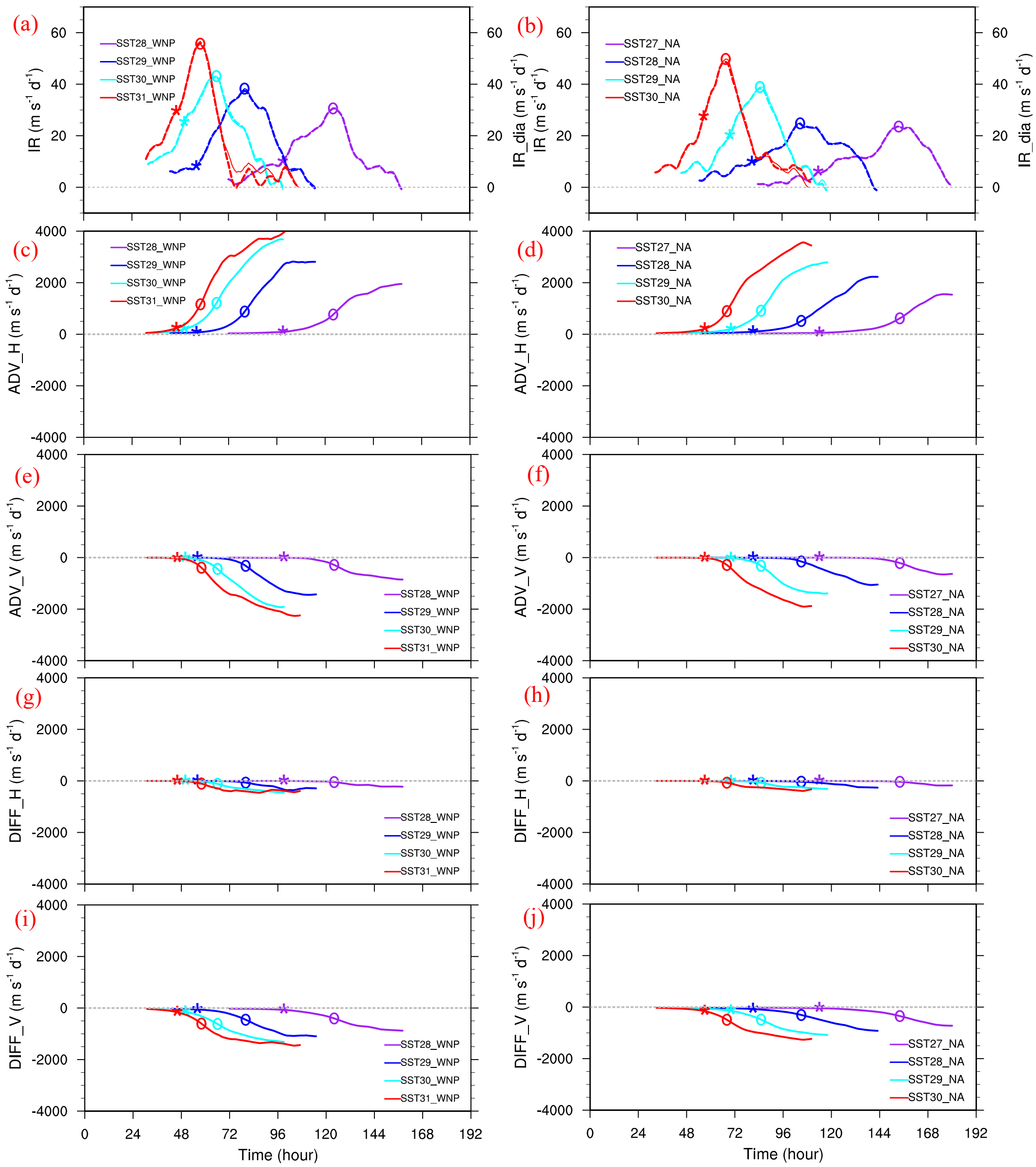

Figure 5. (a,b) Time series of the simulated IR (solid curves) and diagnosed IR based on Eq. (3) (dashed curves) averaged below 500 m. Note that the solid curves are mostly under the dashed curves. (c–j) Time series of the diagnosed IR averaged below 500 m due to (c,d) radial vorticity flux, (e,f) vertical advection, (g,h) radial diffusion, and (i,j) vertical diffusion including surface friction. Only results during the primary intensification period after the initial adjustment are shown. The asterisk and circle on each curve mark the time of the peak RMW contraction rate and the time of the peak simulated IR, respectively.

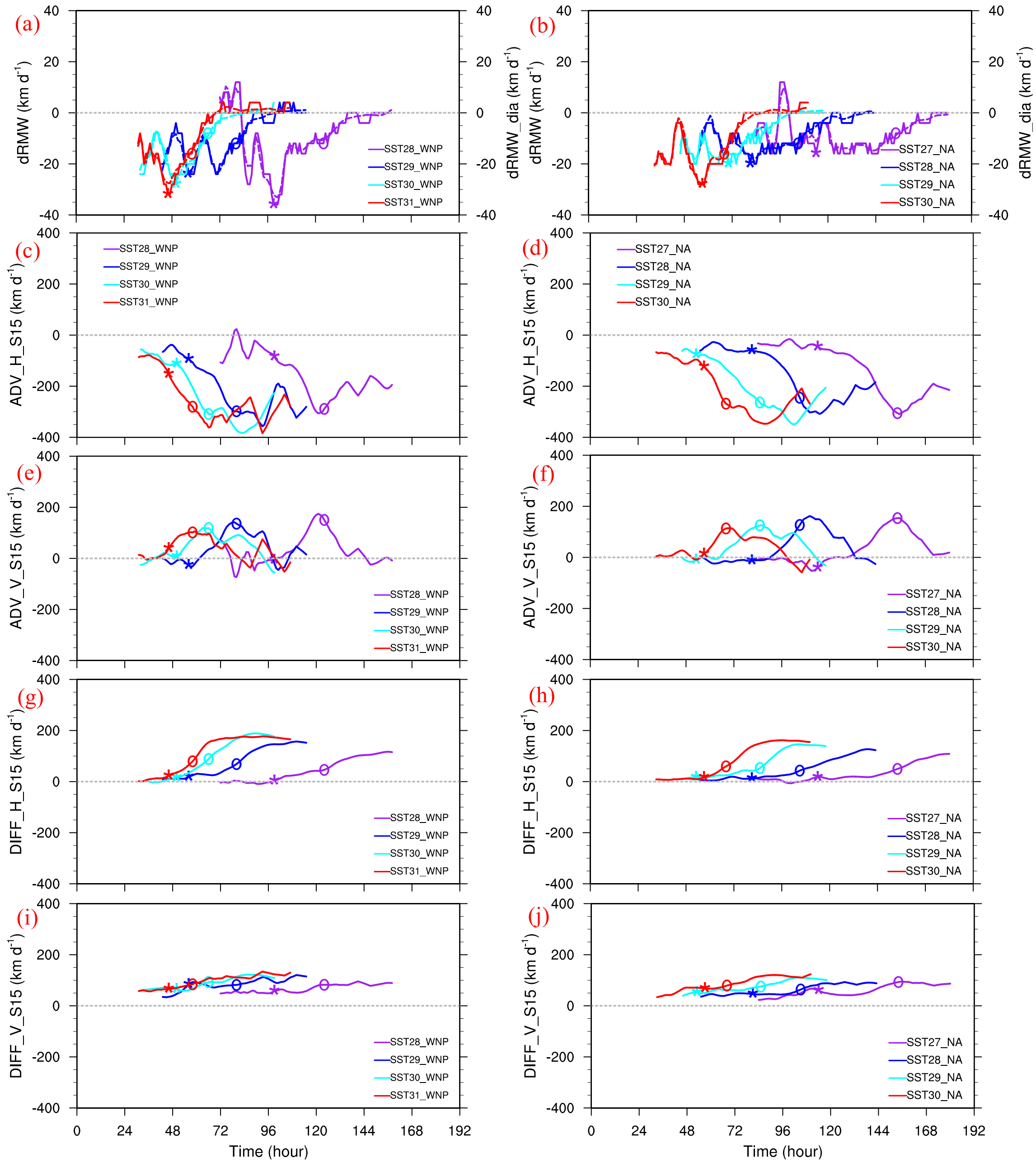

Figure 6. (a,b) Time series of the simulated tendency of RMW (solid curves) and diagnosed tendency of RMW based on Eq. (5) (dashed curves) averaged below 500 m. (c–j) Time series of the contributions of the radial gradient of tangential wind tendency to the RMW tendency averaged below 500 m due to (c,d) radial vorticity flux, (e,f) vertical advection, (g,h) radial diffusion, and (i,j) vertical diffusion including surface friction. Only results during the primary intensification period after the initial adjustment are shown. The asterisk and circle on each curve mark the time of the peak RMW contraction rate and the time of the peak simulated IR, respectively.

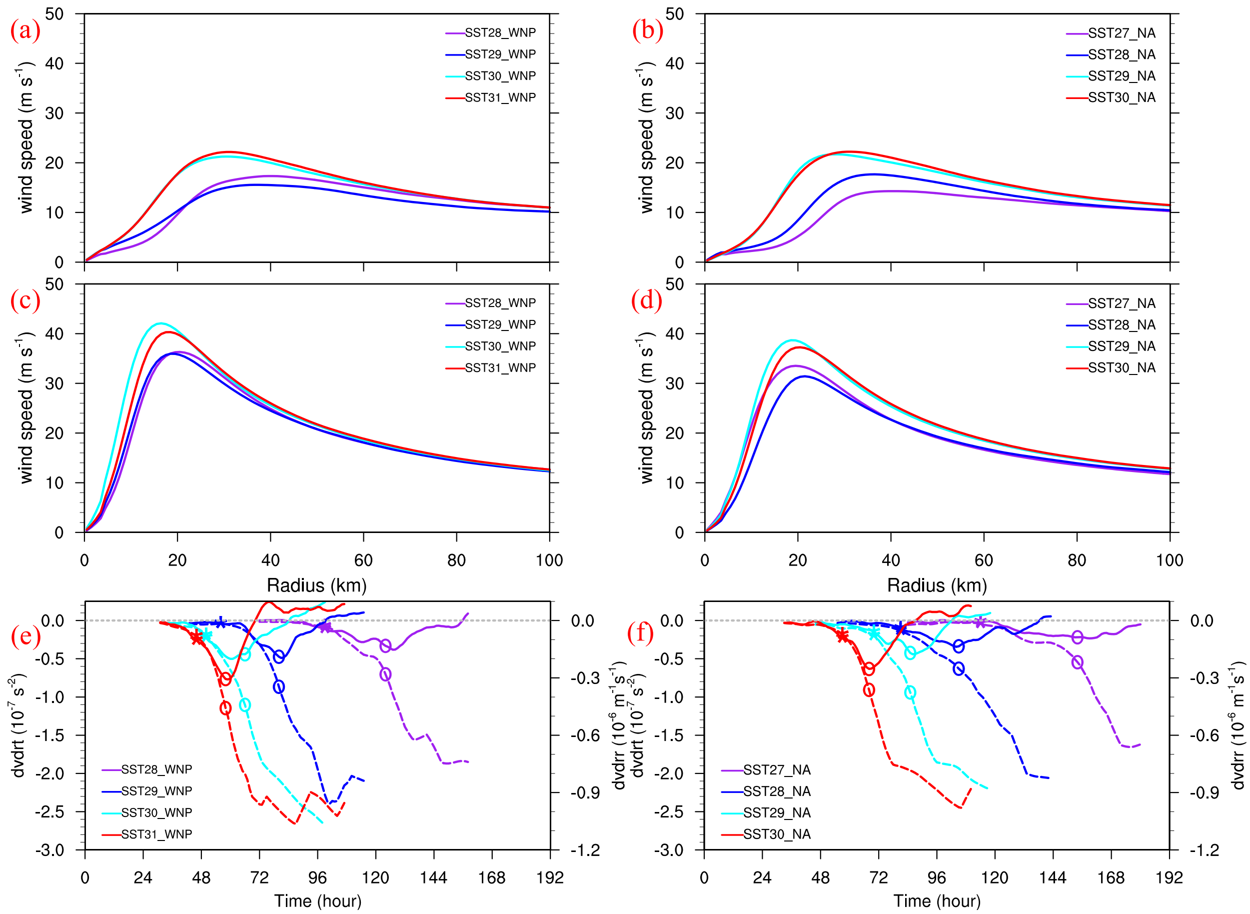

Figure 7. (a,b) Radial profile of tangential wind speed averaged below 500 m at the time of the peak RMW contraction rate. (c,d) As in (a,b), but at the time of the peak simulated IR. (e,f) Time series of the radial gradient of tangential wind tendency (dvdrt ;solid curves) and the curvature of the radial distribution of tangential wind at the RMW (dvdrr; dashed curves). The asterisk and circle on each curve mark the time of the peak RMW contraction rate and the time of the peak simulated IR, respectively.

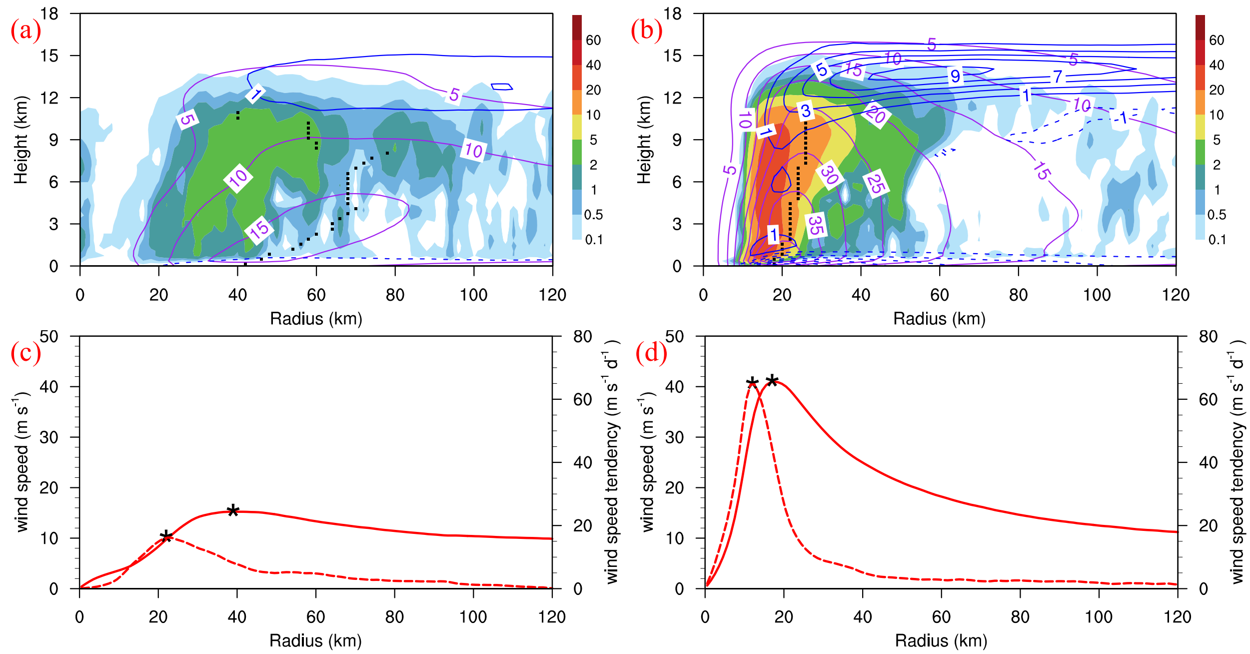

Figure 8. (a,b) Radial-vertical cross sections of the composite diabatic heating rate (shading; K h^{-1}), tangential wind speed (purple contours; at an interval of 5 m s^{-1}), and radial wind speed with negative value dashed (blue contours; at an interval of 2 m s^{-1}) at the time of (a) the peak RMW contraction rate and (b) the peak simulated IR. The dotted black line shows the location of the RMW. (c,d) Radial profile of tangential wind speed (solid) and tendency of tangential wind speed in the subsequent 6 h (dashed) averaged below 500 m at the time of (c) the peak RMW contraction rate and (d) the peak simulated IR. The asterisk marks the radius of the corresponding peak value.